BNL-223438-2022-JAAM

High power density soft x-ray GaAs photodiodes with tailored spectral response

D. Donetski, S. Hulbert

To be published in "Semiconductor Science and Technology"

August 2022

Photon Sciences

Brookhaven National Laboratory

U.S. Department of Energy

USDOE Office of Science (SC), Basic Energy Sciences (BES) (SC-22)

DISCLAIMER

PAPER • **OPEN ACCESS**

High power density soft x-ray GaAs photodiodes with tailored spectral response

To cite this article: Dmitri Donetski *et al* 2022 *Semicond. Sci. Technol.* **37** 085024

OPEN ACCESS
IOP Publishing
Semiconductor Science and Technology
Semicond. Sci. Technol. **37** (2022) 085024 (12pp)
https://doi.org/10.1088/1361-6641/ac7c88

High power density soft x-ray GaAs photodiodes with tailored spectral response

Dmitri Donetski[1], Kevin Kucharczyk[1], Jinghe Liu[1], Ricardo Lutchman[1], Steven Hulbert[2], Claudio Mazzoli[2], Christie Nelson[2] and Boris Podobedov[2,*]

[1] Department of ECE, Stony Brook University, Stony Brook, NY 11794, United States of America
[2] Brookhaven National Laboratory, Upton, NY 11973, United States of America

E-mail: boris@bnl.gov

Received 30 March 2022, revised 17 June 2022
Accepted for publication 28 June 2022
Published 13 July 2022

Abstract

GaAs photodiode arrays have been designed for non-destructive monitoring of x-ray beam position in soft coherent beamline front ends in synchrotron light sources. A shallow p-on-n junction was employed to reduce the device photocurrent density to optimize the operation with beam power densities up to 20 W mm^{-2}, mainly coming from hard x-rays. With this approach, the photocurrent is primarily defined by the excess carriers generated by low-energy x-ray photons absorbed near the detector surface. The p–n junction structures were grown by molecular beam epitaxy and processed into 64-element linear photodiode arrays. The devices were characterized first in the visible range with a high-power Ar-ion laser and then tested in the soft and hard x-ray regions up to 10 keV at two beamlines of the National Synchrotron Light Source II. The responsivity was measured to be 0.16 A W^{-1} at 0.7 keV and 0.05 A W^{-1} at 6 keV in agreement with modeling. At higher x-ray energies the measured responsivity was lower than predicted in the framework of the carrier diffusion model; a possible explanation is discussed.

Keywords: x-ray, GaAs, photodiodes, MBE

(Some figures may appear in colour only in the online journal)

1. Introduction

Synchrotron science is essential to advance our understanding of the laws of nature and drive technological breakthroughs. In particular, soft x-ray imaging at nanometer scale sheds light on chemical bonding, electronic structure, magnetism, and correlations. Some examples include tomographic studies of catalysis to optimize the efficiency of photosynthesis cells [1], imaging motion of topological spin states for ultra-low power information storage, classical and quantum computing [2], imaging ion drift and diffusion in Li-based batteries, memristors [3], visualization of the organization and dynamics of subcellular metabolism for engineering biofuels [4], and understanding of coupled excitations in complex oxides leading to high temperature superconductivity [5]. The fundamental resolution limit for coherent soft x-ray imaging achievable in synchrotron beamlines originates from the finite stability of electron and photon beams. The quality of data produced by these beamlines is highly dependent on their soft x-ray beam control: both high positional beam stability and wavefront control are required at the sample position. In this respect, diagnostics such as x-ray beam position monitors (XBPMs) are critical for evaluating and controlling photon beams delivered

* Author to whom any correspondence should be addressed.

by modern, highly coherent sources. Especially important are the front-end XBPMs, located upstream of the first optical element in a beamline, and thus called 'white-beam'. Given their location, they allow to separate the perturbations coming from the source from those due to beamline optics, and thus offer the opportunities of selective optimizations and dedicated feedback systems. Photoemission-based XBPMs, which typically use metal blades placed into the outside portions of the beam, work well for high-power hard x-ray beams and are routinely utilized at the front ends of hard x-ray beamlines. Such XBPMs, however, if installed into coherent beamlines would produce significant wavefront distortion, therefore, novel non-invasive devices with high spatial resolution are needed.

To tackle the above challenges, our team is presently developing a novel soft x-ray BPM (sXBPM) device for non-invasive monitoring of beam position in the front ends, targeting coherent soft x-ray beamlines in synchrotron light sources [6]. At the core of our device are moveable GaAs detector arrays placed in the outer portion of the x-ray beam to allow us to infer micron-level variations in beam position from the pixel photocurrents. This approach derives from the vastly superior responsivity of semiconductor detectors in the soft x-ray range compared to metals. In semiconductors, the energy of a single x-ray photon is transferred to many photoelectrons. The number of photoelectrons generated can be estimated by dividing the incident photon energy by the electron–hole pair creation energy, i.e. the energy difference between the two bands with the highest transition probability. For GaAs this constant is about 4 eV [7], so, for instance, a 1 keV photon generates up to 250 photoelectrons which results in the detector responsivity of up to 0.25 A W^{-1}. Our approach is to place high-responsivity semiconductor detectors further away from the beam axis to avoid interference with the central portion of the beam, which is utilized by the beamline experiments.

The detector arrays in sXPBM need to operate with high incident power and, consequently, under high thermal load. Source photon power densities greater than kW cm^{-2} levels exist in the front ends of typical modern soft x-ray synchrotron beamlines. The source spectra for soft x-ray beamlines extend to the hard x-ray range and the maximum power load levels are dominated by the high energy portion of these spectra. At these power levels, semiconductor detectors with a broad spectral response would operate at extreme photocurrent densities on the order of kA cm^{-2}. This, however, describes only one regime of the sXPBM operation when the beamline is tuned to deliver the lowest energy photons. At the other extreme, the power densities are much lower, while the radiation is narrow-band and the source spectrum is limited to the soft x-ray range. This regime requires the sXBPM detectors to have a soft x-ray response.

While many wide-gap semiconductors, including CdTe, SiC, GaN and diamond, could be explored for this application, GaAs was selected due to its reproducibility, reliability and robustness for high-yield manufacturing and mature processing technology. Specifically, GaAs-based devices have been shown to operate reliably at extreme current densities and temperatures. Molecular beam epitaxy (MBE)-grown

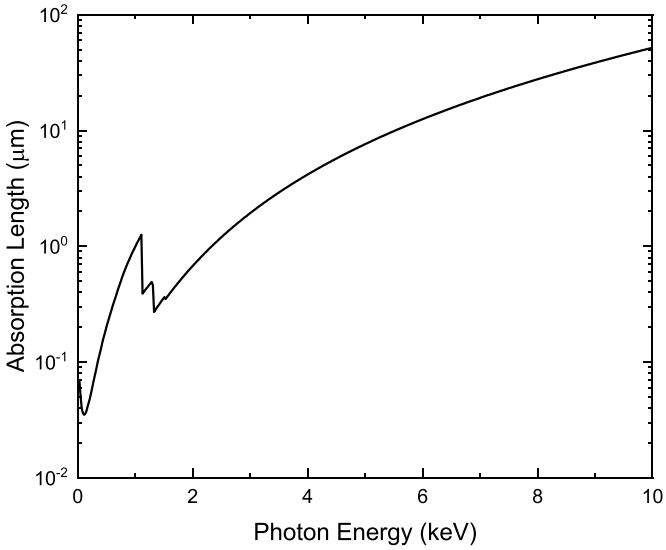

Figure 1. The absorption length versus x-ray photon energy in GaAs.

GaAs-based laser structures have demonstrated 100 000 h operation with a kA cm^{-2} scale current densities and junction temperatures up to 80 °C [8, 9]. The relatively wide energy band gap of GaAs is beneficial for sXBPM operation under high thermal load. GaAs photodiodes have been successfully used in many other applications of direct relevance to sXBPMs. The use of GaAs and AlGaAs photodiodes for the detection of soft x-ray photons has been demonstrated earlier [10–18]. High power GaAs photovoltaic devices have been employed in optical-to-electrical energy conversion [19, 20].

The sXBPM device prototype will be installed in the first optical enclosure (FOE) of the 23-ID canted undulator beamline at the National Synchrotron Light Source II (NSLS-II). As defined by the undulator parameters and the specifics of the device location, the minimum spectral coverage of sXBPM detectors should span from 650 eV to at least 2 keV. It is also necessary to sharply limit the responsivity at higher x-ray energies, to reduce the high photocurrent density mentioned earlier. Details for the expected x-ray beam power densities and spectral contents can be found in appendix A.

Figure 1, plotted using the data from [21], shows that soft x-rays are absorbed in a thin layer near the surface of GaAs. In other semiconductor materials the absorption lengths are similar [21]. A short absorption length for soft x-rays implies the use of epitaxial technology for fabrication of a p–n junction detector with high structural quality of the top layer.

For this project we fabricated GaAs p–n junction structures by MBE. These choices are justified by the maturity of the MBE growth method and subsequent processing technology of GaAs-based devices as well as the possibility of being able to shape the spectral response of the devices via control of the carrier transport properties of the GaAs/AlGaAs heterostructures. MBE technology offers high structural quality of the epitaxial material and precise control of the layer thicknesses and doping levels, both of which are especially important for soft x-ray absorption.

As explained in appendix A, when the beamline undulator source is tuned to the lowest fundamental photon energy, the radiation intercepted by sXBPM has the highest power density and is dominated by high harmonics of undulator radiation which extend into hard x-ray region. To reduce the photodetector current density in this regime, we utilized a thin p-on-n structure. In this case, the collection of excess carriers generated by hard x-ray photons is primarily limited by the hole diffusion length defined by the substrate doping. The majority of excess carriers generated by hard x-ray photons at longer distances from the surface recombine on the way to the p–n junction, without contributing to the photocurrent.

In this work, the GaAs p–n junction structures grown by MBE were processed into linear arrays of mesa devices with various sizes. The device responsivity was measured to be 0.16 A W^{-1} at 0.7 keV photon energy and to decrease as a function of increasing (harder) photon energy, to 0.05 A W^{-1} at 6 keV and 0.004 A W^{-1} at 10 keV. The linearity of the device response versus excitation power density was verified by testing the responsivity with a high-power Ar-ion laser up to a power density value of 200 W cm^{-2}.

2. Device fabrication

The shallow p–n junction structures were grown by a solid-source MBE system Gen-930 on (001) oriented GaAs substrates doped with silicon. The structures were produced by epitaxial growth of a 0.2 μm thick layer of GaAs doped to the level of $p = 8 \times 10^{17}$ cm^{-3} on the top of a 0.2 μm thick undoped layer grown on the substrate, which is nominally doped to the level of $n = 1 \times 10^{18}$ cm^{-3}. The p-doping was made with beryllium. The hole concentration was verified by measuring the Hall effect in a 1 μm thick p-doped layer grown on a semi-insulating GaAs substrate. The wafers were processed into 0.8 μm deep mesa structures obtained by wet chemical etching and passivated with silicon nitride. Figure 2(a) shows a schematic cross-section of the device. One half of the mesa area had an open surface (marked A in figure 2) while another half was covered by metal (marked B in figure 2).

Due to relative transparency of metals in the hard x-ray range compared to lower energies, the responsivity in the hard x-ray range was provided by the entire mesa area while in the soft x-ray and visible/infrared (IR) ranges the responsivity was defined by the open surface of the mesa. The minority holes from the depletion region and n-substrate reach the p-doped region which results in a positive charge. This charge creates an electric field pushing excess holes into the top metal contact to restore the neutrality. The excess holes which reach the open surface window travel laterally in the p-doped layer to the metal contact. Thus, the excess carriers generated primarily by hard x-ray photons under the open surface side A, had to travel laterally in a thin p-doped GaAs layer to side B for collection by the top metal contact. According to modeling, the undepleted part of the top layer had a rather small thickness of $d = 0.1$ μm, thereby limiting the p-layer cross-section which would yield high lateral current density from unwanted hard x-ray photons. The suppression of hard x-ray responsivity helped to avoid extreme photocurrent densities in the p-layer due to the lateral nature of hole transport.

The lower energy x-ray photons are primarily absorbed in the p-layer and the depletion region due to shorter absorption lengths (figure 1). The minority electrons from the p-doped region and the depletion region reach the n-doped substrate creating an excess of negative charge. This charge results in pushing electrons towards the n-contact.

For electrical characterization, the devices were fabricated with mesa dimensions of 12 × 5, 16 × 12, 18 × 18 and 96 × 66 μm^2, referred to as small (S), medium (M), large (L), and extra-large (XL) photodiodes, respectively, with a mesa pitch of 10, 20, 30 and 125 μm for S, M, L and XL devices, respectively. The mesa structures were obtained by wet chemical etching. Using a Trion Plasma Enhanced Chemical Vapor Deposition system, a 0.3 μm thick silicon nitride insulation layer was grown at $T = 250$ °C on the top surface. Afterwards, windows in this dielectric layer, smaller in lateral dimensions than the mesa dimensions, were etched out using the same system. The p-contact metal layers on the epi-side consisted of 20 nm Ti, 100 nm Pt, and 200 nm Au fabricated by a Temescal BJD1800 e-beam deposition system. Figure 2(b) shows a photo of an XL mesa device. An open window with dimensions $L \times D = 50 \times 60$ μm^2 was left in the top metallization layer to provide the device responsivity in the soft x-ray and visible ranges. The epi-side metal had the patterns for 32- and 64-element photodiode arrays with 200 × 200 μm^2 pads used for wire bonding. The substrate was lapped and polished down to 180 μm. The standard n-contact consisting of Ni/Au/Ge/Ni/Au layers with the thicknesses described in [22] was deposited on the substrate side. The samples were annealed in a 5% H_2 forming gas for 30 s at 400 °C. To facilitate soldering, another set of Ti/Pt/Au metal layers with thicknesses similar to those on the epi-side were deposited over the annealed Ni/Au/Ge/Ni/Au contact. The wafers were cleaved into 1 mm wide bars with the photodiode arrays mounted with indium on the ceramic carriers with 32 leads.

3. Electrical and optical device characterization

The photodiode *I*–*V* characteristics were measured with a Keithley 4200 parameter analyzer (figure 3(a)). The diode shunt resistance was determined at the reverse bias voltage of 50 mV. The shunt resistance was found to scale proportional to the effective mesa area, ranging from 30 MΩ for XL devices to 3 GΩ for S devices (figure 3(b)).

The effective mesa side length was taken to be greater than the fabricated mesa side by hole diffusion length to account for collection of minority holes from the peripheral area around the mesa. The shunt resistance was found to scale linearly with the mesa area, indicating a negligible impact of the surface leakage current.

The device responsivity was measured with a high-power Ar-ion laser at the wavelength of 514 nm. The laser beam was

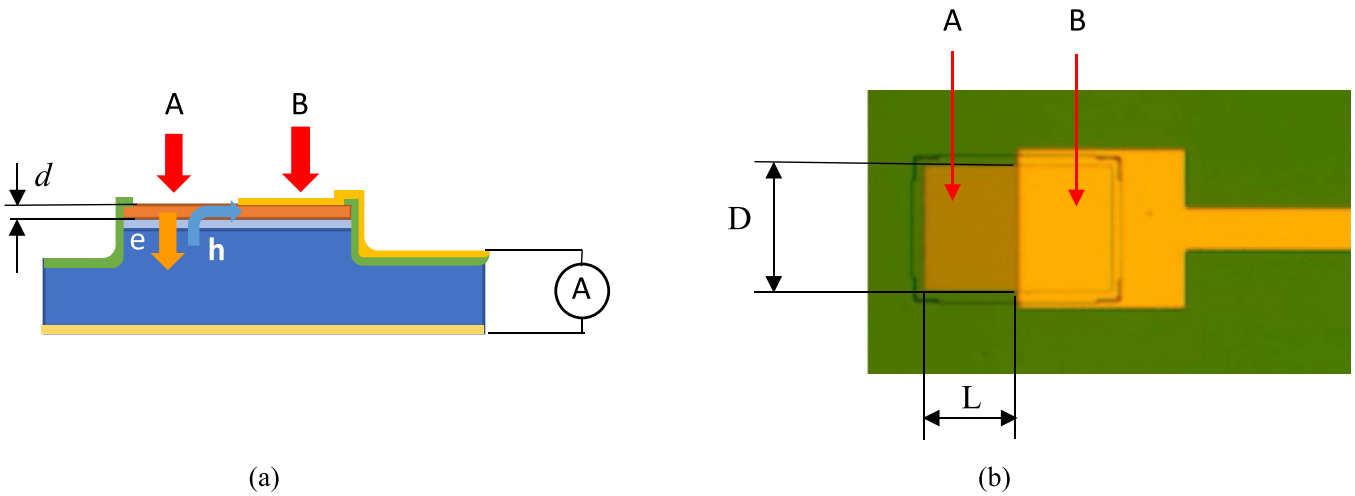

Figure 2. The schematic device cross-section along with a circuit diagram (a) and the top view photo (b) of the XL photodiode array. The red arrows show incident photon fluxes for the open surface (A) and the metallized (B) areas of the mesa, respectively. The photocurrent was measured in the photovoltaic mode (zero DC bias voltage) using a transimpedance amplifier shown schematically with an ammeter symbol. The orange arrow marked 'e' shows the direction of electron flow into the n-type substrate. The blue arrow marked 'h' shows the direction of hole flow into the p-layer of thickness d. For area A the hole flow continues along the p-layer to the metallized area B.

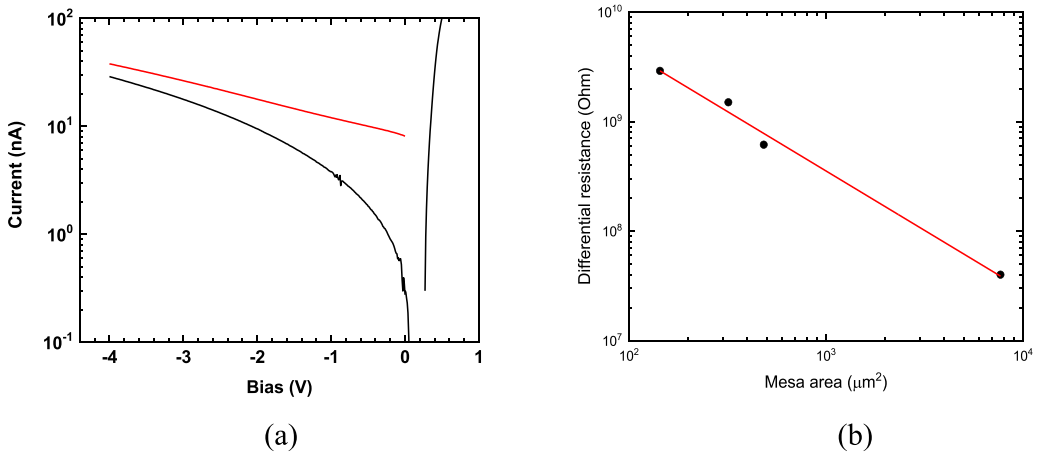

Figure 3. Electrical characterization of the photodiodes: (a) I–V characteristics of XL devices under ambient light (black lines) and with an LED illumination (red line) and (b) the differential resistance versus mesa area determined at the reverse bias of 50 mV.

modulated with a chopper. The laser power was attenuated and measured with a calibrated silicon detector. The photodiode AC current was measured in the photovoltaic mode (zero DC bias voltage) with a transimpedance amplifier Femto DLPCA-200 and a lock-in amplifier Stanford Research SR830. At the laser wavelength of 514 nm, corresponding to a photon energy of 2.4 eV, the photon absorption length in GaAs is 0.1 μm [23] which is the same as for 330 eV x-rays (figure 1). The responsivity at 514 nm was found to be $R_{2.4\text{eV}} = 0.09$ A W^{-1} which is similar to the data reported for GaAs photodiodes [24]. The GaAs reflection coefficient at 514 nm was taken to be RFL $= (n-1)^2/(n+1)^2 = 38\%$ with the refractive index $n = 4.22$ [25]. Assuming that excess carriers generated at 2.4 and 330 eV have similar transport and the normal incidence surface reflection coefficient in the soft x-ray range approaches zero, the device responsivity at 330 eV was estimated to be $R_{330\text{eV}} = R_{2.4\text{eV}}/(1 - \text{RFL}) \times 2.4/4.148 = 0.084$ A W^{-1}. Here, 4.148 eV is the electron–hole pair creation energy in GaAs [7].

The response of the XL mesa devices was measured versus the excitation power of the Ar-ion laser up to a power density level of 200 W cm^{-2} (figure 4(a)). This indicates that the devices with a 50 μm mesa size should demonstrate a constant responsivity vs. power density at 330 eV photon energy (soft x-ray) up to power density levels of at least 2 W mm^{-2}.

The device spectral responsivity was measured in the IR and visible ranges (symbols in figure 4(b)). In the IR range the absorption lengths are longer and similar to those in the hard x-ray range. Thus, the efficiency of collection of excess carriers in the IR range provides the data for modeling of the device efficiency in the hard x-ray range. The GaAs photodiode responsivity spectrum was obtained with a Nicolet Magna

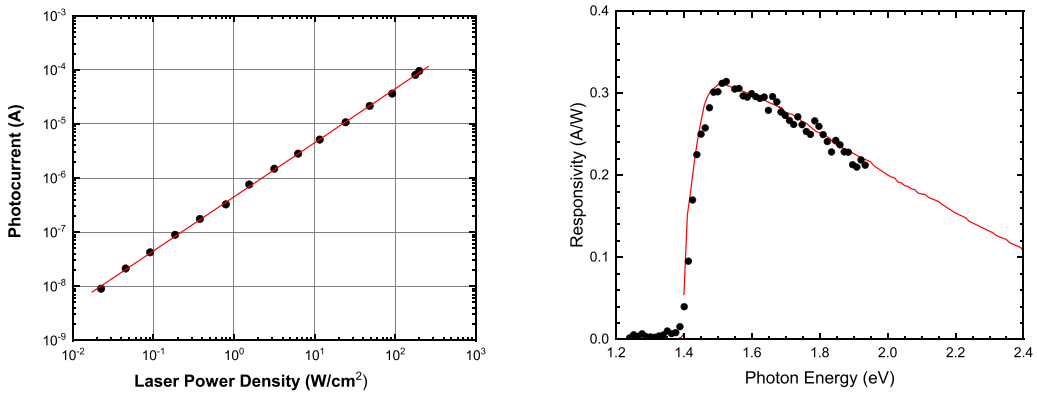

Figure 4. (a) The device response versus a 514 nm laser power density and (b) the experimental near-infrared responsivity spectrum of GaAs and a fit with a 3 μm hole diffusion length (solid line). The latter defines the device responsivity in the hard x-ray range discussed in the text.

860 Fourier Transform IR spectrometer with an internal white light source. The white light source emission spectrum was determined with a calibrated silicon detector FDS-010 from Thorlabs.

4. Modeling of the device responsivity

Our modelling of the device responsivity spectrum originates from [26]. In this approach, for the doped regions, the excess electron and hole concentrations were found from the continuity equations with the carrier generation term in the form $\Phi\alpha\exp(-\alpha\, d)$, where Φ is the incident photon flux and α is the absorption coefficient. Due to pinning of the Fermi level at the GaAs surface and the energy band bending near the surface, for the boundary conditions of the p-doped region we used zero excess carrier concentration. The excess carriers generated in the surface region with band bending were considered to be recombined without contributing to the device responsivity. For the boundaries of the n-doped region we used zero excess carrier concentration at the interface with the depletion region and its zero gradient at the substrate surface. The photocurrents of minority electrons and holes due to diffusion of excess carriers to the depletion region were found as the products of the corresponding gradients of excess carrier concentrations and the diffusion coefficients at the interface with the depletion region. The photocurrent from the depletion region was found by integration of the number of generated excess carriers. The responsivity terms were found by dividing the photocurrent from the corresponding region by the photon flux multiplied by the photon energy.

The device responsivity was described by the sum of three terms shown in equations (1)–(3): (a) responsivity term R_p due to photons absorbed in the neutral part of the top p-doped region; (b) responsivity term R_w due to photons absorbed in the depletion region; and (c) responsivity term R_n due to photons absorbed in the n-type substrate. The expressions for these responsivity terms, in A/W units, are:

$$R_\mathrm{p} = \frac{1}{E}\frac{(1-\mathrm{RFL})\,\alpha L_\mathrm{n}\exp(-\alpha t)}{\alpha^2 {L_\mathrm{n}}^2 - 1} \times \left\{ \alpha L_\mathrm{n}\exp(-\alpha d) - \frac{1-\cosh\left(\frac{d}{L_\mathrm{n}}\right)\exp(-\alpha d)}{\sinh\left(\frac{d}{L_\mathrm{n}}\right)} \right\} \quad (1)$$

$$R_\mathrm{w} = \frac{1}{E}(1-\mathrm{RFL})\exp(-\alpha(d+t))\left[1-\exp(-\alpha w)\right] \quad (2)$$

$$R_\mathrm{n} = \frac{1}{E}(1-\mathrm{RFL})\exp(-\alpha(d+w))\frac{\alpha_\mathrm{s} L_\mathrm{p}}{\alpha_\mathrm{s} L_\mathrm{p}+1}. \quad (3)$$

Here, E is the photon energy, α and α_s are the absorption coefficients in the epilayer and the n-doped substrate, respectively, t is the thickness of the depleted part of the surface layer due to the pinning of the Fermi level within the energy gap, d is the thickness of the neutral top layer with p-type conductivity, w is the depletion region width, and L_n and L_p are the electron and hole diffusion lengths in the p-type and n-type layers, respectively. For the layer thicknesses and doping levels of the grown structures specified above, the following parameters were used: $w = 0.3$ μm, $d = 0.1$ μm, and $t = 0.05$ μm. Similar equations were obtained and successfully used in [27–29].

Due to long absorption lengths, the IR light is primarily absorbed in the n-type substrate. Therefore, the device responsivity is defined by hole transport from the substrate to the p–n junction characterized by hole diffusion length, L_p. The absorption spectrum in the heavily doped substrate was obtained from the absorption of undoped GaAs, considering the Moss-Burstein effect which affects the absorption near the energy gap [30]. The level of electron concentration in the substrate was verified by measurement of the GaAs substrate conductivity by the Van der Pauw method. The contacts in the

corners of the GaAs sample cleaved from the wafer were made by alloying indium. The electron mobility in the substrate was taken to be 3000 $cm^2\ V^{-1}\ s^{-1}$ [31]. The substrate concentration was found to be $1 \times 10^{18}\ cm^{-3}$.

The hole diffusion length was determined to be $L_p = 3\ \mu m$ from the best fit of the model to the measured responsivity spectrum, where the hole diffusion length was a fit parameter (solid line in figure 4(b)). Similar hole diffusion lengths for silicon-doped GaAs substrates from the mid-10^{17} to the low-10^{18} range were reported in [32].

Equations (1)–(3) and the carrier transport data obtained with optical characterization were used in modeling of the device responsivity in the optical range (red line in figure 4(b)) and x-ray region in section 7 below using the electron–hole creation energy of 4.148 eV substituted for the photon energy *E*.

5. Device responsivity measurements in soft x-ray

These measurements were performed at the TARDIS endstation of CSX (Coherent Soft x-ray, 23-ID-1) beamline at NSLS-II. Only the largest size devices (XL) were measured. Their active mesa area, defined by the fabricated window in the top dielectric insulation layer, was $50 \times 60\ \mu m^2$. The relatively large active area allowed for more accurate determination of the device responsivity under the conditions of a relatively low soft x-ray flux in the configuration used, described below.

The photodiode arrays were mounted on a customized 8″ vacuum flange (figure 5(a)) which was then attached to one of the available chamber ports (figure 5(b)). The chamber was pumped out to Ultra High Vacuum (UHV) level. The soft x-rays were directed towards the arrays (at normal incidence) via reflection from a WSi_2/Si multilayer mirror grown by NSLS-II deposition lab at BNL [33, 34], installed at the sample location in the center of the chamber (figure 5(b)).

The multilayer mirror reflected photons with an energy of 696 eV, and its mounting provided a means of scanning of the x-ray beam over the location of the photodiode arrays. A reference AXUV100G (Opto Diode Corp.) silicon diode detector with an active area of $10 \times 10\ mm^2$ and a responsivity of 0.26 A W^{-1} at 700 eV [35] was positioned in front of the arrays on a rotating stage. The beam power was measured with the silicon photodiode intercepting the entire beam. Upon completion of the beam power measurements, the rotating stage with the silicon diode was moved out of the way to allow for unobstructed illumination of the GaAs photodiodes.

The photoelectric response was sequentially measured in three GaAs photodiodes using the following procedure. A single photodiode was connected to a preamplifier, then the beam was aligned with this photodiode by rotating the multilayer mirror. The device photocurrent was recorded while scanning the beam with respect to the photodiode in two orthogonal directions, θ and μ, indicated in figure 5(b). This resulted in the angular map of the beam shown in figure 6(a). A cross-section of the beam spatial distribution in the θ direction is shown in figure 6(b). The peak device photocurrent was measured to be 12.5 nA. The flux intercepted by a single photodiode in a certain position was obtained by integrating the beam spatial distribution image in figure 6(a) and referencing it to the total beam power measured with the silicon diode detector. All three photodiodes that were measured showed similar responsivities, equivalent to 61 ± 2% of the responsivity of the reference silicon diode. In absolute units the measured photodiode responsivity at 0.7 keV is therefore 0.16 A W^{-1}. Separate measurements with varying incoming flux confirmed the linearity of the device response as illustrated in figure 6(c).

6. Responsivity measurements in hard x-ray

Photodiode responsivity in the photon energy range from 6 to 10 keV was measured at the NSLS-II 4-ID (ISR) beamline for the devices of XL size. The array carrier was mounted on the sample stage of the 6-circle diffractometer, which allowed for the precise motion of the photodiodes in the horizontal (x) or vertical (y) directions, transverse to the propagation direction of monochromatic x-ray beam (figure 7(a)). The range of motion was sufficient to scan a mesa across the x-ray beam, thereby substantially varying the flux intercepted by the photodiode. The x-ray beam was focused at the array location and was approximately Gaussian, aligned with the axes, ranging in size from $320 \times 45\ \mu m^2$ to $490 \times 60\ \mu m^2$ full width at half maximum (FWHM), depending on the energy. The x-ray energy was varied in 0.5 keV steps, set by tuning the 4-ID undulator source and Si (111) double crystal monochromator (relative bandwidth $\sim 10^{-4}$). At each energy, a device photocurrent was measured during the horizontal (figure 7(b)) and vertical (figure 7(c)) scans, while the total x-ray beam flux was simultaneously measured with an ion chamber located upstream of the array carrier. Maximum photocurrents at each energy were in the range from 1 to 7 μA. The photon flux measured with an ion chamber increased monotonically as a function of x-ray energy, from 1×10^{11} ph s^{-1} at 6 keV to 2.2×10^{12} ph s^{-1} at 10 keV.

For a pixel intercepting x-ray power *P* and measuring photocurrent *I*, the responsivity, in A/W, is defined by

$$R = I/P. \tag{4}$$

If the total beam flux and its transverse distribution are known, then the intercepted power can be easily calculated. For instance, for a rectangular pixel of size $w \times h$ located at the center of the x-ray beam with photon energy E (eV) and total flux Φ (photons s^{-1}), the intercepted power P (W) is given by

$$P = e\,E\,\Phi\,\mathrm{erf}\left(\frac{w}{2\sqrt{2}\sigma_x}\right)\mathrm{erf}\left(\frac{h}{2\sqrt{2}\sigma_y}\right), \tag{5}$$

where σ_x, σ_y are the respective rms sizes and erf denotes the error function.

A slightly more complicated expression arises for a displaced pixel, which, combined with equation (4) can be used to fit each photocurrent scan, like the ones shown in figures 7(b) and (c). These fits allowed us to determine the responsivity as well as other unknown parameters, specifically

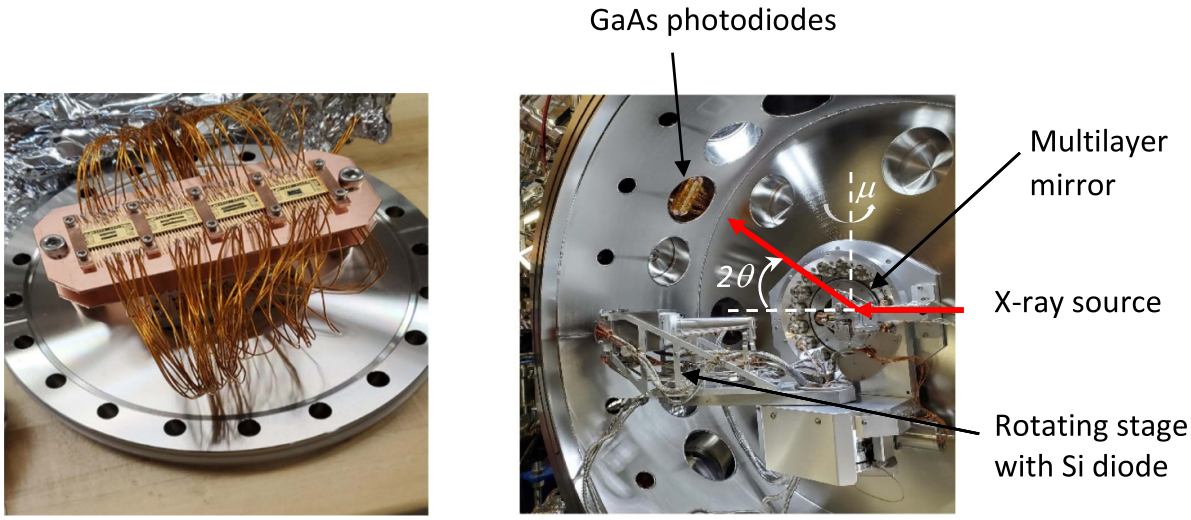

Figure 5. (a) GaAs photodiode arrays on the copper plate mounted on the custom $8''$ flange and (b) photo of the TARDIS chamber (inner radius ∼0.6 m). Red arrows show the direction of the x-ray beam. The x-ray beam, reflected by the multilayer mirror installed as the sample in the center of the experimental station, was scanned across the diode array by moving two angles: θ and μ.

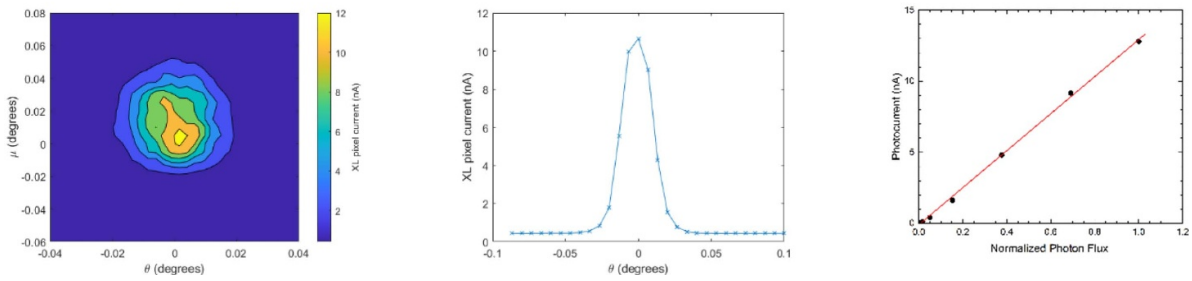

Figure 6. (a) Beam distribution at 696 eV obtained from scanning the x-ray beam across the device under test. (b) The response of the device under test versus the multilayer mirror tilt angle θ. (c) The response of the GaAs photodiode as a function of photon flux. To determine the device response, the background was subtracted.

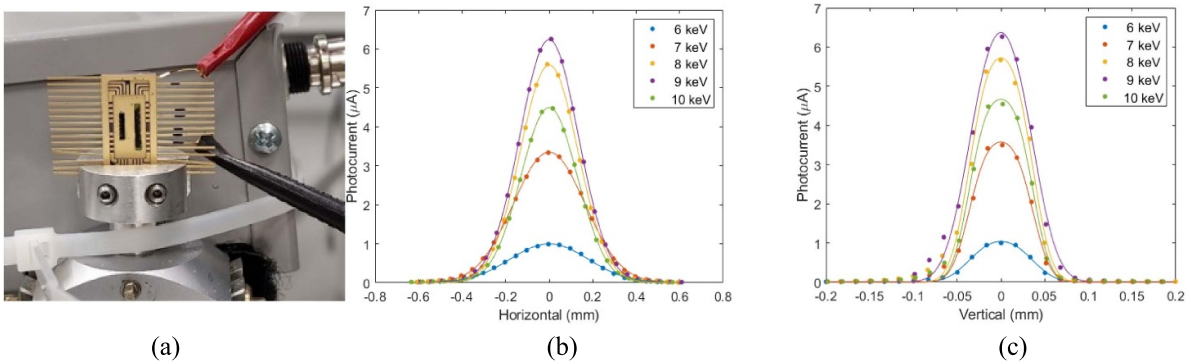

Figure 7. GaAs photodiode arrays in the carrier mounted in the ISR beamline diffractometer (a); photodiode response for the horizontal (b) and vertical (c) scans at the specified x-ray energies. Symbols indicate measured values, lines show fit results, as described in the text.

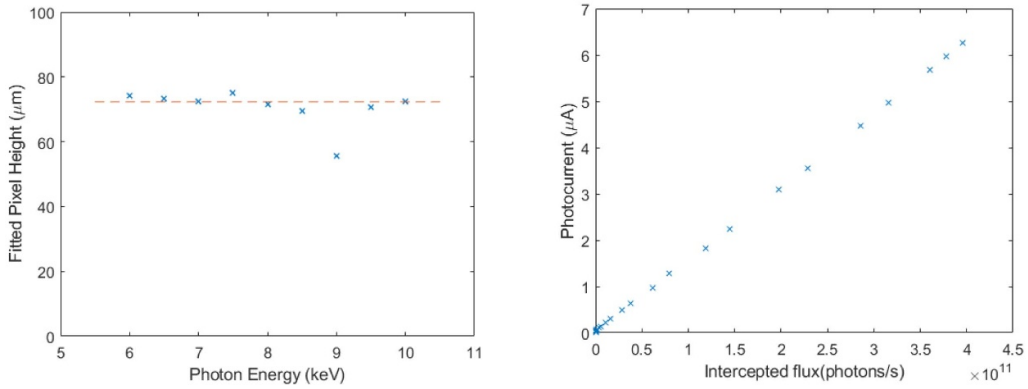

(a) (b)

Figure 8. (a) Fitted effective pixel height for one of the pixels. Broken line denotes the median value of 72.3 μm. (b) Photocurrent vs intercepted flux from 9 keV horizontal scan shown in figure 7(b).

σ_x, σ_y, and the relative position of the mesa to the x-ray beam center.

We first performed these fits for the vertical scans. Due to the vertical size of the x-ray beam being significantly smaller than the vertical mesa dimension, we were able to accurately determine the vertical mesa dimension by fitting each scan, and then averaging the result for all values of energy. The final value for the effective vertical mesa dimension was found to be $h = 72.3$ μm (figure 8(a)). The fact that this effective height is larger than the corresponding mesa dimension of 66 μm is explained by the collection of excess carriers from an area which exceeds the fabricated mesa dimensions by the hole diffusion length in each direction. Note that, in contrast to soft x-ray, the dielectric and metal layers are essentially transparent to 6–10 keV photons. Therefore, the active mesa size was defined by the actual fabricated mesa dimensions of 96×66 μm^2 with the addition of the hole diffusion length in each direction.

Due to isotropy of the diffusion process in GaAs, the final responsivity values were found from fits with fixed $w = 102.3$ μm, $h = 72.3$ μm. Examples of the fitted scans are shown in figures 7(b) and (c). Well-fitted shapes of the photocurrent scans confirmed the linearity of the device response with change of the incident x-ray flux. This is also illustrated more directly in figure 8(b) for one of the scans.

Fitted values σ_x, σ_y were consistent with the rms beam sizes measured separately by scanning the positions of narrow horizontal and vertical slits located just upstream of the ion chamber. For the photocurrent measurements these slits were set wide open. Separately, the slit measurements confirmed beam asymmetry in the vertical plane at some energies, where the beam was not optimally focused. This feature is also visible in some traces of figure 7(c). Our later analysis confirmed that this asymmetry, affecting only the tails of the beam for a subset of energy values, had a negligible effect on the measured responsivity.

The final responsivity values obtained from the fitting described above are plotted in figure 9. There are four points at each energy, corresponding to x and y scans performed for each of two different photodiodes. The small spread among the points measured at each photon energy confirms the reproducibility of the scan procedure during the measurement as well as similar responsivity values for different devices.

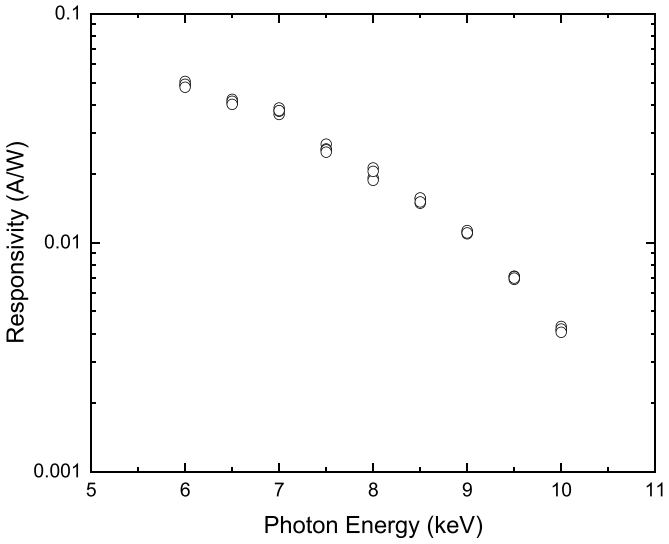

Figure 9. Responsivity of the GaAs photodiodes measured at the ISR beamline.

7. Comparison of measured and simulated spectral responsivities

Figure 10 shows the spectral responsivity of the photodiodes in the x-ray range. Measurement results, described earlier in sections 3, 5 and 6 are shown by symbols. The solid square at the photon energy of 330 eV represents the responsivity obtained with the Ar-ion laser with a similar absorption length and the correction for the differences in the photon energies (4.148 eV vs 2.4 eV) and refraction coefficients. The solid triangle at 696 eV represents the measurements at the CSX beamline, while the open circles show the responsivity measured at the ISR beamline.

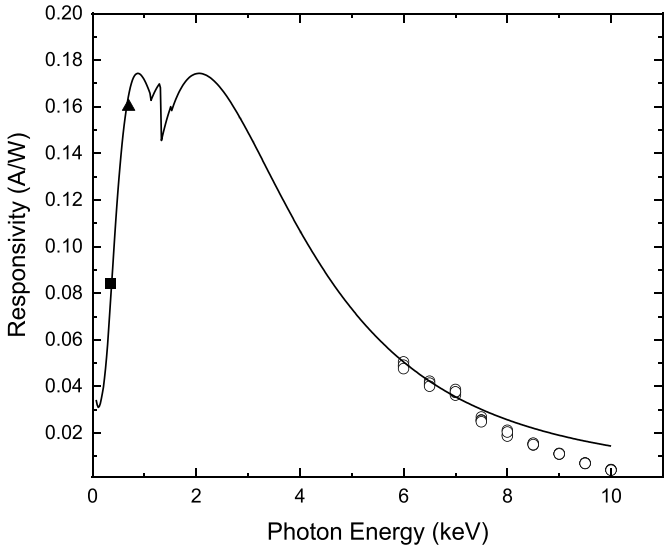

Figure 10. The measured (symbols) and simulated (line) device responsivity vs. photon energy. The line represents the model given by equations (1)–(3). The solid square shows the projected x-ray responsivity at 330 eV based on the data obtained with the Ar-ion laser at 2.4 eV. The solid triangles and open circles show the responsivity obtained by direct measurements at CSX 23-ID-1 and ISR 4-ID beamlines, respectively.

Modeling of the responsivity spectrum was performed with equations (1)–(3), using the absorption length for GaAs shown in figure 1. The photon energy E in equations (1)–(3) was replaced with the electron–hole pair creation energy of 4.148 eV taken from [7]. The reflection from the surface was neglected ($R = 0$). The responsivity at 0.33, 0.7 and 6 keV are found to match the model.

A decrease in measured responsivity relative to the model values was observed for photon energies greater than 7 keV, by an amount approximately proportional to the photon energy. Besides systematic effects including the impact of air ionization and calibration uncertainties, the observed deviation in responsivity above 7 keV could potentially be attributed to the impact of the momentum transfer from photons to the excess carriers and lattice. This effect is known as the photon drag effect, which is observed in semiconductors in the IR range [36]. In the x-ray range, the momentum of photon is orders of magnitude greater than in the IR range, and, therefore, it may impact the excess carriers from the substrate toward the depletion region near the surface, thus contributing to the energy dependence of the responsivity in the hard x-ray range.

8. Summary and future work

We designed, fabricated, and tested GaAs photodiode arrays for use in a novel XBPM for coherent soft x-ray beamlines. The design has met the unique needs of this application, including sufficient responsivity from sub-keV to a few keV photon energies and the ability to handle large x-ray power densities, while producing manageable photo-current density. This detector response was accomplished by using a shallow p–n junction obtained by epitaxial growth of p-layer on an n-substrate. In this design, the excess holes are collected with the lateral current flow which could lead to high current density to the side metal contact. The shallow p–n junction design has allowed us to minimize the hard x-ray responsivity, which results primarily from hole diffusion between the n-type substrate and the p–n junction. The corresponding reduction of hole collection significantly lowered the device photocurrent density in the top p-layer.

The GaAs diodes have been tested with an Ar-ion laser, confirming response linearity up to power densities of 200 W cm^{-2}, as well as in low-power soft and hard x-rays up to 10 keV. The measured x-ray responsivity was found to be reasonably close to the expectation within the framework of the hole diffusion model. In particular, the low responsivity in the hard x-ray range, required for proper sXBPM performance, was confirmed. In the 6–10 keV range, the observed responsivity vs photon energy decrease was even steeper than in the model, which is beneficial for the reduction of the photocurrent density in sXBPM. We speculate that this discrepancy could be attributed to the photon drag effect. Finally, our measurements of the response of different pixels confirmed the expected pixel-to-pixel reproducibility.

Diode arrays of this type, albeit with a modified layout, will be incorporated in an sXBPM assembly which is expected to be installed in the first optics enclosure of the NSLS-II 23-ID beamline later this year. This will be followed by an extensive program of characterizing sXBPM performance in high-power x-ray beams.

Future detector-related work will include fabrication and testing of the design utilizing GaAs/AlGaAs heterostructures optimized for integration with 64-channel current-input Analog to Digital converters for efficient data acquisition and processing with Field Programmable Gate Arrays.

Data availability statement

The data that support the findings of this study are available upon reasonable request from the authors.

Acknowledgments

We are grateful for the support of the Accelerator & Detector Research Program of the Scientific User Facilities Division, Office of Basic Energy Sciences, Office of Science of the U.S. Department of Energy (DOE). We thank Nathalie Bouet for providing the multilayer mirror sample. This research used beamlines 4-ID (ISR) and 23-ID-1 (CSX) of the NSLS-II, a DOE Office of Science User Facility operated for the DOE Office of Science by Brookhaven National Laboratory under Contract No. DE-SC0012704.

Appendix A. Power and photon spectral densities at sXBPM

Coherent soft x-ray beamlines use permanent magnet undulators as the source of synchrotron radiation. Undulators

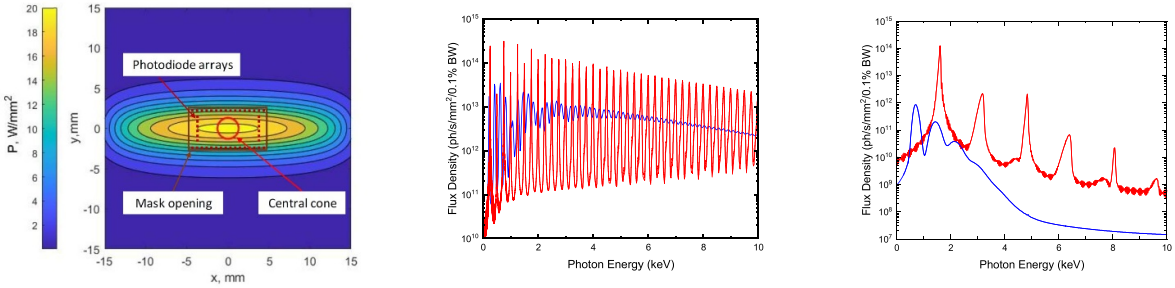

Figure A1. (a) Transverse distribution of the radiation power density at the sXBPM when the undulator fundamental harmonic is tuned to 250 eV ($K = 3.46$). Photons outside the mask opening do not reach the sXBPM. (b) Photon spectral flux for the undulator fundamental harmonic tuned to 250 eV ($K = 3.46$). The flux is plotted on axis, $x = y = 0$ (red) and in the corner of the mask opening at $(x, y) = (4.8, 2.5)$ mm (blue). (c) Same for the case of the undulator fundamental harmonic tuned to 1615 eV ($K = 0.4$).

provide radiation in the form of harmonics, with the central wavelengths λ_n given by (see e.g. [37]):

$$\lambda_n = \frac{\lambda_u}{2n\gamma^2}\left(1 + \frac{K^2}{2} + \theta^2\gamma^2\right), \tag{A1}$$

where λ_u is the undulator period, γ is the electron's Lorentz factor, θ is the angle between the electron beam axis and the observation point, and the undulator parameter is given by $K = 0.934B\,(\mathrm{T})\,\lambda_u\,(\mathrm{cm})$, where B is the amplitude of the on-axis magnetic field. The spectral content of the radiation is controlled by adjusting the undulator gap, which changes the magnetic field and, consequently, the undulator parameter K. A monochromator tuned to the fundamental or some other low odd undulator harmonic λ_n ($n = 1, 3, 5, \ldots$) further limits the typical bandwidth to $\sim 10^{-4}$. The coherent photons transmitted through the monochromator are limited to the central portion of the undulator beam, usually referred to as the 'central cone'.

The sXBPM will be installed upstream of the monochromator (i.e. in a white x-ray beam). During user operations, the sXBPM detector arrays will only interact with the photons outside of the central cone, as shown in figure A1(a). During studies, the sXBPM will also be used to characterize the spatial distribution of the radiation, including on-axis.

The sXBPM will be installed in the FOE of the 23-ID canted undulator beamline at the NSLS-II, which operates in the photon energy range of 0.25–2 keV. The undulator source of the coherent branch of the beamline (CSX) ($L_u = 2$ m long, $\lambda_u = 4.9$ cm permanent magnet undulator) is tunable for the fundamental photon energies, $E_1 = h\,c/\lambda_1$, from 250 to 1615 eV, corresponding to the K values of 3.46 and 0.4, respectively. Due to spatial and other constraints stemming from installing the sXBPM prototype into an operating beamline, the installation location was chosen 26 m downstream of the center of the undulator. This location happens to be 1 m downstream of an FOE aperture mask with rectangular opening dimensions of 9.525×5.2 mm^2. The maximum length of the sXBPM diode arrays was therefore chosen to be 1 cm.

Properties of synchrotron radiation relevant to sXBPM design were analyzed using analytical approaches along with the well-established numerical codes SRW [38] and SPECTRA [39]. In the most commonly used undulator operating mode with a horizontal linear polarization, the synchrotron radiation power density on-axis at the sXBPM location ranges from 1.6 W mm^{-2} at $K = 0.4$ to 20 W mm^{-2} at $K = 3.46$. As K increases, the corresponding horizontal beam size grows from about 2 to 8 mm FWHM while the vertical beam size remains approximately constant at 3 mm FWHM. Thus, at $K = 3.46$, the arrays maximally retracted away from the center to the inner edge of the mask will be exposed to power densities on the order of 20 W mm^{-2} (figure A1(a)).

Figures A1(b) and (c) illustrate that, at a fixed K, the radiation away from the axis shifts towards longer wavelengths as described by the θ^2-term in equation (A1). Separately, at $K = 0.4$, the spectral content is dominated by the fundamental harmonic with the central photon energy 1615 eV on-axis, which shifts down to 678 eV at the corner of the mask opening. These two values, with some margins due to the harmonic bandwidth and other factors added in, define the minimum detector spectral coverage range of 650–2 keV.

In contrast, as is clear from figure A1(b), at $K = 3.46$, the radiation spectrum consists of many harmonics, which extend well into hard x-ray. For instance, on-axis, 80% of power comes in the energy range of 2–16 keV. Because this regime is also characterized by the highest radiation power density of up to 20 W mm^{-2}, it is required to sharply limit the detector responsivity at x-ray energies beyond a few keV, to reduce the photocurrent density.

Appendix B. Thermal modelling

Exposure of the GaAs photodiode array to a high-power x-ray flux raises a question about temperature rise and some potential issues for the device operation at elevated temperatures. In order to address this, we performed COMSOL [40] simulations of the temperature elevation of the photodiode array under exposure of a 50 μm wide strip to the highest expected x-ray power density of 20 W mm^{-2}. (In the mechanical design of sXBPM [41], the width of the exposed strip will be controlled by a tungsten screen upstream of the device, and the chosen width value could be considered as typical.) In the

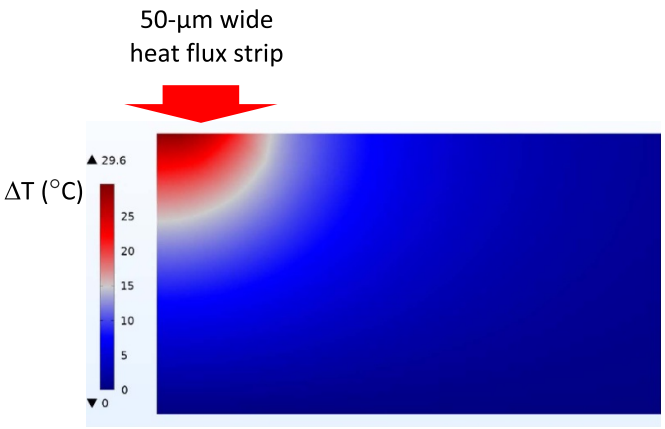

Figure A2. Temperature elevation distribution over a 180 μm thick GaAs substrate with the photodiodes in the upper left corner exposed to the power density of 20 W mm^{-2} applied on a 50 μm wide strip. The temperature at the bottom surface of the GaAs substrate is held constant.

simulations the temperature at the bottom surface of a 180 μm thick GaAs substrate was held constant. The heat flux was applied from the top side of the GaAs substrate as shown in figure A2.

As follows from our modeling, the elevation of the photodiode temperature can approach 30 °C. Then, for instance, a 25 °C temperature maintained at the bottom of the GaAs substrate would cause the photodiode temperature to reach a maximum of 55 °C. Due to the finite thermal resistance of the GaAs device mount, the actual temperatures at the bottom surface of the GaAs substrate and the p–n junction, respectively, could be somewhat higher. While the device mount design is still evolving, several candidate designs analyzed so far have all resulted in the photodiode temperature of less than 80 °C. On the other hand, long-term device operation at $T = 80$ °C and at a high current density has been demonstrated [8, 9], therefore we believe our prototype design is acceptable.

One of the effects which arises with elevated temperatures is the thermally generated current, which can be simply estimated. Thermal generation of excess carriers is dominated by the contribution from the depletion region. The current density from the depletion region at room temperature can be estimated as $J_d = e\, n_i W/2\tau \sim 4$ nA cm^{-2}, where $e = 1.6 \times 10^{-19}$ C is the electron charge, $n_i = 2 \times 10^6$ cm^{-3} is the GaAs intrinsic carrier concentration, $W = 0.3$ μm is the depletion region width, $\tau = 1$ ns is an estimate of the effective carrier lifetime. The intrinsic carrier concentration in GaAs at $T = 80$ °C was taken to be 10^9 cm^{-3} [42]. With these parameters, the thermally generated current density at $T = 80$ °C is estimated to be 2 μA cm^{-2}. On the other hand, the integration of the device responsivity in figure 10 with the maximum x-ray spectral flux at the detector location in figure A1(b) results in photocurrent densities on the order of tens of A cm^{-2}. Therefore, the photocurrent would be 6–7 orders of magnitude higher than the thermally generated current, so the latter can be safely neglected.

ORCID iDs

Dmitri Donetski https://orcid.org/0000-0003-2472-1606
Boris Podobedov https://orcid.org/0000-0002-6042-9971

References

[1] Wise A M, Nelson Weker J, Kalirai S, Farmand M, Shapiro D A, Meirer F and Weckhuysen B M 2016 *ACS Catal.* **6** 2178–81
[2] Fert A, Reyren N and Cros V 2017 *Nat. Rev. Mater.* **2** 17031
[3] Sun W, Gao B, Chi M, Xia Q, Joshua Yang J, Qian H and Wu H 2019 *Nat. Commun.* **10** 3453
[4] Roth M S *et al* 2019 *Plant Cell* **31** 579–601
[5] Chen X M *et al* 2019 *Nat. Commun.* **10** 1435
[6] Liu J, Kucharczyk K, Lutchman R, Donetski D, Eng C, Hulbert S L, Mazzoli C and Podobedov B *12th Int. Particle Acc. Conf. IPAC2021* (*Campinas, SP*) (https://doi.org/10.18429/JACoW-IPAC2021-MOPAB121)
[7] Bertuccio G and Maiocchi D 2002 *J. Appl. Phys.* **92** 1248–55
[8] Michaud J, Béchou L, Veyrié D, Laruelle F, Dilhaire S and Grauby S 2016 *IEEE Photonics Technol. Lett.* **28** 665
[9] Souto J, Pura J and Jimenez J 2018 *MRS Commun.* **8** 995
[10] Ardashev E N, Gorokhov S A, Polkovnikov M K, Lobanov I S and Vorobiev A P 2011 *Nucl. Instrum. Methods Phys. Res.* A **648** S8
[11] Lioliou G and Barnett A M 2016 *Nucl. Instrum. Methods Phys. Res.* A **836** 37
[12] Barnett A M, Bassford D J, Lees J E, Ng J S, Tan C H and David J P R 2010 *Nucl. Instrum. Methods Phys. Res.* A **621** 453
[13] Lees J E *et al* 2011 *J. Instrum.* **6** C12007
[14] Lees J E, Bugby S L, Boieb L and Scoulara C 2014 *J. Instrum.* **9** P05003
[15] Veale M C, Bell S J, Duarte D D, French M J, Hart M, Schneider A, Seller P, Wilson M D, Kachkanov V and Lozinskaya A D 2014 *J. Instrum.* **9** C12047
[16] Sun G C, Makham S, Bourgoin J C and Mauger A 2007 *Nucl. Instrum. Methods Phys. Res.* A **571** 300–3
[17] Hatsui T and Graafsma H 2015 *IUCrJ* **2** 371
[18] Denes P and Schmitt B 2014 *J. Synchrotron Radiat.* **21** 1006
[19] Khvostikov V, Sorokina S, Potapovich N, Khvostikova O, Shvarts M, Timoshina N and Andreev V 2015 *AIP Conf. Proc.* **1679** 13002
[20] Oliva E, Dimroth F and Bett A W 2008 *Prog. Photovolt. Res. Appl.* **16** 289–95
[21] Henke B L, Gullikson E M and Davis J C 1993 *At. Data Nucl. Data Tables* **54** 181–342
[22] Bruce R A and Piercy G R 1987 *Solid State Electron.* **30** 729–37
[23] Schaefer S T, Gao S, Webster P T, Kosireddy R R and Johnson S R 2020 *J. Appl. Phys.* **127** 165705
[24] Newport Corporation (available at: www.newport.com/p/818-BB-45)
[25] Aspnes D E, Kelso S M, Logan R A and Bhat R 1986 Optical properties of $Al_xGa_{1-x}As$ *J. Appl. Phys.* **60** 754–67
[26] Djuric Z, Livada B, Smiljanic M, Matic M and Lazic Z 1989 *Infrared Phys.* **29** 1–7
[27] Cheknane A and Benouaz T 2009 *J. Semicond.* **30** 72001
[28] Blaj G, Kenney C J, Segal J and Haller G 2017 (arXiv:1706.01429v1)
[29] Kucharczyk K, Zhao J, Kipshidze G, Belenky G, Bane S and Svenssson A 2022 *Appl. Phys. Lett.* **120** 14101

[30] Hudait M K, Modak P and Krupanidhi S B 1999 *Mater. Sci. Eng.* B **56** 1–11
[31] Rode D L 1975 *Semiconductors and Semimetals* vol 10, ed R K Willardson and A C Beer (New York: Academic) p 1
[32] Hwang C J 1969 *J. Appl. Phys.* **40** 3731
[33] Conley R, Bouet N, Biancarosa J, Shen Q, Boas L, Feraca J and Rosenbaum L 2009 *Proc. SPIE* **7448** 74480U
[34] Bouet N, Macrander A T, Maser J, Chu Y S, Zhou J, Nazaretski E, Yan H, Huang X and Conley R 2019 *J. Nanosci. Nanotechnol.* **19** 575–84
[35] Opto Diode Corporation (available at: https://optodiode.com/pdf/AXUV100GDS.pdf)
[36] Alperovich V L, Belinicher V I, Novikov V N and Terekhov A S 1981 *JETP Lett.* **33** 557–60
[37] 2004 *The Science and Technology of Undulators and Wigglers, Oxford Series on Synchrotron Radiation* ed J Clarke (Oxford: Oxford University Press)
[38] Chubar O and Elleaume P 1998 *Proc. EPAC'98* (*Stockholm*) pp 1177–9
[39] Tanaka T and Kitamura H 2001 *J. Synchrotron Radiat.* **8** 1221–8
[40] COMSOL Multiphysics® v. 6.0 (Stockholm: COMSOL AB) (available at: www.comsol.com)
[41] Eng C, Donetski D, Hulbert S, Liu J, Mazzoli C and Podobedov B *11th Int. Conf. on Mech. Eng. Design of Synchr. Rad. Equip. and Instrum. (MEDSI2020)* (https://doi.org/10.18429/JACoW-MEDSI2020-MOPC01)
[42] Kemerley R T, Wallace H B and Yoder M N 2002 *Proc. IEEE* **90** 1059–64